

- ⁷ D M Le Vine, A J Griffis, C T Swift, T J Jackson, 'ESTAR: A synthetic aperture microwave radiometer for remote sensing applications', Proc. IEEE **82**, 12, pp 1787-1801, (1994)
- ⁸ C Edelson, 'Applications of synthetic aperture radiometry', Proc. IGARSS, pp 1326-1328, (1994)
- ⁹ K Komiyama, 'Indoor experiment of two-dimensional supersynthesis radiometer', Proc. IGARSS, pp 1329-1331, (1994)
- ¹⁰ H A Maillot, 'A cross beam interferometer for high resolution microwave sensing', Proc. IEEE Aerospace App. Conf., pp 77-86, (1993)
- ¹¹ M martin-Neira, J. Font-Rossello, 'Mechanically scanned interferometric microwave radiometer using sub-arraying', ESTEC Internal Report, XR1/108.97/MMN, October 1997.
- ¹² Harvey A R, Greenaway A H, Camps A, Corbella I, Torres F, Bara J, Martin-Neira M, 'Millimetre-wave aperture synthesis radiometry for snow and ice mapping', Proc. Int. Conf. Geosci. Rem. Sen., Hamburg, 28 June-2 July 1999
- ¹³ A R Harvey, 'Report on passive aperture synthetic mm-wave imaging from unmanned airborne vehicles', Report to DERA DAPS/AH/42/99/0.A, October 1999
- ¹⁴ C S Ruf, C T Swift, A B Tanner, D M Le Vine, 'Interferometric synthetic aperture radiometry for the remote sensing of the Earth', IEEE Trans. GeoSci. Rem Sens. **26** 5, pp 597-611 (1988)
- ¹⁵ A R Thompson, J M Moran and G W Swenson, 'Interferometry and synthesis in radio astronomy', Wiley, pp 162-165, (1986)
- ¹⁶ A Camps, J Bará, F Torres, I Corbella, J Romeu, "Impact of antenna errors on the radiometric accuracy of large aperture synthesis radiometer", Radio Science, **32**, 2, pp 657-668 (1997)
- ¹⁷ F Torres, A Camps, J Bará, I Corbello, R Ferrero, "On-board phase and modulus calibration of large aperture synthesis radiometers: study applied to MIRAS", IEEE Trans. Geosci. Rem. Sen., **34**, 4, pp 1000-1009, (1996)
- ¹⁸ F Torres, A Camps, J Bara, I Corbella, 'Impact of receiver errors on the radiometric accuracy of large aperture synthesis radiometer', Radio Science, **32**, 2, pp 629-641 (1997)
- ¹⁹ C S Ruf, "Error analysis of image reconstruction by a synthetic aperture interferometric radiometer", Radio Sci., **26**, 6, pp 1419-1434, 1996
- ²⁰ A B Tanner, C T Swift, 'Calibration of a synthetic aperture radiometer', IEEE Trans. GeoSci. Rem. Sen. **31**, 1, pp 257-267, (1993)
- ²¹ D E Weissman, D M Le Vine, 'The role of mutual coupling in the performance of synthetic aperture arrays', Rad. Sci., **33**, 3, pp 767-779, (1998)
- ²² F Torres, A Camps, J Bara, I Corbella, R Ferrero, 'On-board phase and modulus calibration of large aperture synthesis radiometers: study applied to MIRAS', IEEE Trans. Geosci. Rem. Sen. **34**, 4, pp 1000-1009, (1996)
- ²³ Burnett J G, Erry G R G, Dickson R, McBride R, Gander M, Jones J D C, Blanchard P M, Greenaway A H, Harvey A R, 'Channelled spectrum interrogation of an all fibre broadband interferometric differential strain sensor', European Workshop on Optical Fibre Sensors, **3483**, ch 66, pp 174-178, (1998)
- ²⁴ S Woods, A H Greenaway, A R Harvey, 'Optimal shape sensing using statistically derived basis sets', In preparation
- ²⁵ S Woods, A H Greenaway, A R Harvey, 'Optimal shape reconstruction using modal decomposition', Proc. IOP Conference on Applied Optics and Electronics, Brighton, UK, 16-19 March, pp 145-150, (1998)
- ²⁶ A R Harvey, 'Determination of the optical constants of thin films in the visible by dispersive Fourier transform spectroscopy', Review of Scientific Instruments, **69**, 10, pp 3649-3658, (1998)

coupling in sparse arrays of circular antennas will be smaller than for ESTAR and MIRAS although scattering from the UAV structure and sensor pods may still introduce significant artifacts that will need to be calibrated.

It was noted by Weissman and Le Vine²¹, that displacements of antennas of 0.003λ in the plane of the antenna resulted in errors of 3 K in the reconstructed image and that curvature of 0.01λ along the antenna array introduced similar sized errors. The 0.5° phase accuracy quoted by Camps et al suggests an accuracy of approaching 0.001λ is required in the plane orthogonal to antenna array. It is proposed that the antenna patterns can be measured in the laboratory for a given antenna shape. Real-time measurement of antenna shape once in service will then enable calculation of the actual in-service antenna patterns. The antenna will change shape once in service due to flexing of the UAV.

As a working estimate of the antenna calibration accuracy required, we will assume 0.003λ in the plane of the UAV and 0.001λ out of the plane. These are probably a little in excess of the accuracies actually required (for example the lower mutual coupling between antennas will reduce the sensitivity to in-plane movement). These figures correspond to $10 \mu\text{m}$ and $3 \mu\text{m}$ for the 80 GHz antenna structure. The most suitable method for measuring the mechanical shape of the array is with electrical or optical-fiber strain gauges. Optical fiber strain sensors based on either Bragg gratings or broadband-light interferometry using a superluminescent LED light source²³ can yield high accuracy shape measurement and can be readily integrated into composite structures such as the UAV frame. If necessary a single optical fiber may be used to multiplex many sensors, but as an absolute minimum a single sensor is required for each degree of freedom of a flexible structure^{24,25}. Traditionally interrogation is achieved with moving-mirror Michelson interferometers, but for use on an aircraft no-moving-parts interferometry using channelled spectrum²³ or spatial interferometers²⁶ is more attractive.

Fiber sensors may be imbedded on opposite sides of, for example, the wing, and bending may be measured from the differential strain in each fiber. With white light optical interferometry, 1 nm displacement can be measured²⁶ so that for a 1 m long sensor and a wing 2.75 m long and 5 cm thick, displacements of less than $0.1 \mu\text{m}$ (worst case) can be measured in the plane of the antenna which is equal to about 0.01° . In summary, it is proposed that periodic in-service receiver calibration follows calibration techniques already developed for MIRAS, but real-time calibration of the antenna patterns will also be required. This can be achieved using the G-matrix method developed for ESTAR, but with the addition of real-time measurement of antenna array shape that enables real-time calculation of the antenna-pair impulse response.

6. CONCLUSIONS

It has been shown that it is possible to produce acceptable antenna patterns from a SAIR integrated into a UAV platform, but that simultaneous achievement of acceptable sensitivity and complexity is difficult. Both of these parameters can be improved to tractable levels by the use of very sparse arrays of antennas that produce a sparsely sampled support region. In this paper we have supposed that it is possible to design an antenna array to give the desired sampling distribution in the support region. This may not be possible in general, but optimization techniques should enable appropriate antenna arrays to be designed that are compatible with the real estate available on a UAV. Calibration of a UAV mounted into a flexible structure such as a UAV will be difficult, but given the algorithms and optical fiber shape measurement technology that exists, calibration appears to be a tractable problem.

ACKNOWLEDGEMENT

This work was funded under an extra mural research contract from DERA, Malvern, UK

REFERENCES

- ¹ IEEE Trans, Geosci., Rem. Sen. **36**, special edition, (1998)
- ² N Skou, B Laursen, 'Measurement of ocean wind vector by an airborne, imaging polarimetric radiometer', Rad. Sci., **33**, 3, pp 669-675, (1998)
- ³ R Appleby, R N Anderton, S Price, N A Salmon, G N Sinclair, J R Borrill, P R Coward, P Papakosta, A H Lettington, D A Robertson, 'Compact real-time (video rate) passive millimetre-wave imager', Passive mm-wave imaging technology III, SPIE **3703**, Ch.19, pp.13-19
- ⁴ A.R. Harvey, R. Appleby, P Coward, A H Greenaway, R Anderton, G Hawkins, 'Electronic beam-steering for passive millimetre-wave imaging', Proc. 4th Int. Conf. on mm & submm-waves and applications, SPIE **3465**, San Diego, July 20-23, (1998)
- ⁵ Blanchard P M, Greenaway A H , Harvey A R, Webster K, 'Coherent optical beamforming with passive millimetre wave arrays', J. Lightwave Technology, **17**, 3, pp 418-425 (1999).
- ⁶ M Martin-Neira, J M Goutoule, A Knight, J Claude, J Bara, A Camps, F Torres, I Corbella, A Lannes, E Anterrieu, B Laursen, N Skou, 'Integration of MIRAS breadboard and future activities', pp 869-871, IGARSS (1996)

5. SYSTEM CALIBRATION

Calibration for SAIR systems is considerably more complex than for conventional radiometers and is proving to be one of the greatest obstacles to their deployment. The main difficulties lie in coherently combining complex signals over distances of several meters with accurately known amplitude and phase characteristics. However calibration for SAIR systems is more tractable than for phased-array RADAR, since calibration corrections are applied in computer software rather than microwave hardware. Mounting of a SAIR onto a UAV is a particularly demanding problem, since the antennas will be mounted to the aircraft wings and fuselage, which will undergo significant flexing during UAV operation. Further problems are likely to be experienced due to thermal drift in the SAIR components. Calibration of a UAV-mounted SAIR will require the calibration and real-time software correction of all of these factors, where real-time refers to the rate at which parameters, such as the shape of the antenna array, are changing.

The fundamental parameters that are measured by a SAIR are the set of complex visibility functions for each baseline that is available from the antenna array topology. The measured visibility functions can be written for the n th correlator output as

$$\begin{aligned}
 V'_m + iV'_{Qn} &= V''_m + iV''_{Qn} \\
 &+ K_1 K_2 \int_{-1}^1 \frac{T_B(\xi, \eta)}{\sqrt{1 - \xi^2 - \eta^2}} \tilde{r}_{12}(v\xi + v\eta) F_1(\xi, \eta) F_2^*(\xi, \eta) e^{-2\pi i(v\xi + v\eta)} d\xi d\eta
 \end{aligned} \tag{11}$$

where I and Q subscripts refer to the in-phase and quadrature components, the double-primed terms are bias terms caused by coupling of correlated noise between antennas, K_1 and K_2 are complex calibration constants determined by antenna attenuation, amplifier gain and correlator efficiency, $T_B(\xi, \eta)$ is the two-dimensional temperature distribution we wish to deduce, $\tilde{r}_{12}(v\xi + u\eta)$ is the fringe wash function for correlation between antenna 1 and 2 on baseline $v+u$ and F_1 and F_2 are the complex antenna patterns of antennas 1 and 2. To invert equation (11) and form high quality images of $T_B(\xi, \eta)$, with accurate absolute and relative temperature measurements requires calibration of the unknown terms.

The general principles of calibration of synthetic aperture radiometers have been covered in the literature for MIRAS^{16,17,18} and ESTAR^{19,20,21}. For 1K temperature sensitivity, the net complex amplitude transmission for each correlator should be calibrated to within 1% in amplitude and 0.5° in phase^{16,18}. It is convenient to consider the calibration of the antenna structure and receivers separately. It is proposed here that the calibration methods proposed for MIRAS using noise injection to overlapping subsets of receivers²² should be applied for periodic re-calibration of the receiver and correlator chain. This calibration is with respect to a baseline calibration performed in the laboratory. The calibration interval should be determined by the scale time for drift in the complex gain of the electronics and the signal distribution system. The antenna array will vibrate and its shape needs to be calibrated in real-time. Shape calibration will enable calibration and image reconstruction using the G-matrix technique developed for ESTAR²⁰. The proposed calibration sequence consists of

- Baseline laboratory calibration of the receiver chain using noise injection.
- Baseline laboratory calibration of antenna shape
- Baseline calibration of the combined antenna/receiver chain complex amplitude response via measurement of antenna-pair impulse responses.
- Periodic in-service re-calibration of the receiver chain with respect to the baseline calibration
- Real-time calibration of the antenna shape

Thus calibration consists of baseline calibration followed by in-service re-calibration with respect to this baseline and the receiver and antenna components are calibrated idependently.

It is clear from work on both ESTAR and MIRAS that accurate knowledge of antenna patterns is essential for calibration. Recent reports on ESTAR²¹ indicate that mutual coupling plays a major role in determining the antenna pattern but can be accurately described if only the coupling to the nearest neighbor was included. This may also be the case for the irregular arrays proposed here, although the use of omnidirectional antennas rather than stick antennas will greatly reduce mutual coupling and hence reduce its impact on SAIR calibration. With little need for short baselines in surveillance, the mutual

$$B_{\max} < \frac{c}{D \sin \vartheta_{\max}}$$

(10)

Where c is the speed of light, D is the width of the SAIR aperture and ϑ_{\max} is the maximum angle with respect to the center of the field of view. If greater bandwidths are required so as to yield improved radiometric sensitivity, then the full IF bandwidth must be channelised into frequency bands with bandwidths less than B_{\max} .

4. DESIGN PARAMETERS FOR SAIR TECHNIQUES

In this section we report estimates of parameters for SAIRs designed by each of the three techniques and these are summarized in Table 1 below. Results are presented for two representative UAVs denoted here as simply small UAV and large UAV. The outline of the small UAV is shown in Figure 1(a) and has a wing span of 5.5 m. The larger UAV has a wing span of 14.8 m. They are assumed to be flying at 2,000 m and 6,000 m respectively.

The methods as outlined in section 2 are denoted by numbers 1, 2 and 3. The dimensions of the antennas assumed for each technique are indicated in rows three and four together with the total numbers of antennas required for sampling of the support regions. It is assumed that for the irregular array, about 1,000 sample points in the support region will give adequate sidelobe suppression and this will require about 46 antennas, assuming it is possible to avoid redundancy in the array. The maximum unchannelised bandwidths are determined by the field of view and the width of the antenna array and are given in the seventh row. The calculated radiometric sensitivities are shown in the eighth row under the assumption that the maximum possible integration time can be used. This requires pixel averaging. This will be less than perfect and so radiometric sensitivities will actually be somewhat worse than these values. For snapshot imaging, the integration time is somewhat shorter and the resulting sensitivity is shown in row 9 for method 3.

The most significant aspect of the results is that method 3, which uses an irregular array, enables wide field of view imaging with considerably higher sensitivities and requires much lower complexity (in terms of number of correlators, number of antennas/receivers and required bandwidth). However, sensitivities of 1-2 K are desirable for most passive mm-wave imaging tasks and so the predicted values of about 5 K and 7 K are inadequate. Sensitivity improves in proportion to $1/\sqrt{B\tau}$, so an increase by a factor of about 16 in $B\tau$ will enable these target sensitivities to be attained. The lowest cost route to improving $B\tau$ is by pixel averaging to increase τ . However channelising a wider bandwidth into contiguous bands so as to increase B is also possible and this also promises to reduce sidelobe levels by smearing of the images.

A particularly important parameter is the small number of antennas and receivers required by method 3. Not only does this reduce cost, but the integration of the required feedhorns into the UAV structure is less problematic than for the other methods.

Method	Small UAV			Large UAV		
	1	2	3	1	2	3
Antenna length	0.44	0.44	0.003	0.36	0.36	0.003
Antenna width	0.002	0.1075	0.003	0.002	0.1075	0.003
Total Number of antennas	1,862	47	46	5,962	158	46
Total number of full-band complex correlations	16,220	331	1,000	63,521	1,489	1,000
Maximum single-channel bandwidth (MHz)	63	3,123	63	23	1,160	23
Radiometric sensitivity - no channelisation, maximum integration time (K)	7.6	1.4	0.18	18.0	1.9	0.22
Radiometric sensitivity- no channelisation, snapshot integration time (K)			5.1			7.4
Swath width at Nadir	$\pm 60^\circ$	$\pm 2^\circ$	$\pm 60^\circ$	$\pm 60^\circ$	$\pm 2^\circ$	$\pm 60^\circ$

Table 1 Salient parameters for UV-mounted SAIRS

the improvement in SNR that is in principle possible. In the interests of economy, the number of antennas in this direction can therefore be kept as small as possible without adversely effecting sensitivity.

Now, for an antenna array on a spacing of $2\Delta_x/\lambda$, $2\Delta_y/\lambda$, where Δ_x , Δ_y are integers, we have $N_x=1/\Delta_x\Delta\xi$, $N_y=1/\Delta_y\Delta\eta$ and so we can write, for equal redundancy β in each baseline,

$$\Delta T = (T_B + T_A) \left(\frac{v}{B\beta\Delta_x\Delta\xi\Delta\eta h} \right)^{\frac{1}{2}} w_{rms} \quad (7)$$

The average redundancy per baseline is given by

$$\begin{aligned} \beta &= \frac{n(n-1)}{N_x N_y} \approx \frac{n^2}{N_x N_y}, \\ &= n^2 \Delta_x \Delta_y \Delta\xi \Delta\eta \end{aligned} \quad (8)$$

so the sensitivity may be written as

$$\Delta T = (T_B + T_A) \frac{1}{n\Delta\xi\Delta\eta\Delta_x} \left(\frac{v}{B\Delta_y h} \right)^{\frac{1}{2}} w_{rms} \quad (9)$$

To enable alias-free imaging in the across-track dimension, we will employ $\Delta_x=1$. It is also implied by equation (9) that to minimize ΔT for a given number of receivers/antennas, n , the antenna spacing in the along-track direction should be as great as possible. When the antenna spacing in this direction is greater than $\lambda/2$ (that is, $\Delta_y>1$), aliased images will be introduced. This means that only those pixels closest to $\eta=0$ offer low errors and the effective integration time is reduced. In practice, this results in a halving of the effective integration time and an increase in $\sqrt{2}$ in ΔT . In effect, this entails a trade off of a reduction in the number of expensive receivers for an increase in the number of correlators - a trade off that will reduce the overall system cost and complexity.

In practice, one may be more interested in detecting small objects and improved performance will then be achieved by configuring the antenna array such that there are proportionately more long baselines. This could be achieved by having proportionately greater numbers of antennas towards the ends of the wings of a UAV than the centers. This would result in improved sensitivity at high spatial frequencies and improved detection of small objects. The radiometric sensitivity denoted by equation (5) should therefore be taken as just an approximate guide to performance.

As can be seen from equation (9), improvements in sensitivity can be bought at the expense of increased receiver bandwidth B , increased numbers of antennas, n and improved receiver noise, T_A . The latter is probably the least important parameter to be traded: improvements in sensitivity are marginal for reductions in amplifier noise below the background noise temperature of 300 K. In the medium-to long-term future, the costs of the antennas/receivers in mm-wave aperture synthesis imaging are likely to considerably exceed the costs of the digital correlation hardware. This is an even more important consideration for deployment on a UAV where integration of antennas into the aircraft superstructure places an additional technical difficulty and cost penalty that makes it desirable to minimize their number. It is assumed here that the maximum possible feasible bandwidth will be employed and the minimum number of antennas.

It can be seen from equation (1) and its derivatives that the radiometric sensitivity improves with the square root of the bandwidth of the intermediate frequency (IF). The scale of the synthesized image is proportional to frequency and this limits the maximum instantaneous bandwidth. This is equivalent to stating that temporal coherence must be maintained across the array across the full field of view, which requires the following condition to be satisfied:

$$\Delta T = (T_B + T_A) \left(\frac{\sum_{i=0}^N \frac{1}{r_{i,j}}}{B\tau} \right)^{\frac{1}{2}} w_{rms}, \quad (3)$$

which is the expression used for sensitivity for all subsequent calculations. For uniform weighting $w_{rms}=1$ and for Hamming weighting, as used for the modeling described in this article $w_{rms}=0.63$. This expression is used directly for calculation of the sensitivity of the irregular array (SAIR technique 3), but for the use of regular arrays (techniques 1 and 2), some further simplification is enlightening.

For maximum sensitivity, the integration time τ should be as long as possible. The maximum possible value is the duration that a point on the ground remains within the field of view of a single antenna. For a SAIR mounted to a UAV this is equal to the along-track dimension of the synthesized image divided by the platform speed, which is

$$\tau = \frac{N_y \Delta \vartheta h}{v}. \quad (4)$$

where N_y is the number of pixels formed along the direction of travel, $\Delta \vartheta$ is the FWHM angular resolution in the same direction, h is the height of the platform and v is the speed. The full exploitation of this integration time will require pixel averaging and the tracking of pixels through the synthesized image during the time τ . In practice this will be difficult to efficiently achieve, but equation (4), serves as an upper bound on integration time. A lower bound is the duration for which a point on the ground remains within a resolution cell within the synthesized image and this can be considered the integration time for true snapshot imaging. It will be seen that even with the upper bound on integration time, acceptable sensitivities are difficult to attain and only the SAIR technique 3 appears able to offer acceptable sensitivities from snapshot imaging.

Substituting equation (4) into equation (3) and assuming that the antenna array is configured on a rectangular matrix so that there are $N_x N_y$ baselines gives

$$\Delta T = (T_B + T_A) \left(\frac{v \sum_{i=0}^{N_x} \sum_{j=0}^{N_y} \frac{1}{r_{i,j}}}{BN_y \Delta \vartheta h} \right)^{\frac{1}{2}} w_{rms} \quad (5)$$

Sensitivity can be improved by introducing redundancy into the processing. This means that more baselines than are formed than are required for acceptable image quality, so that averaging of measured visibilities (which are proportional to Fourier image components) results in reduced noise. This is most efficiently achieved by equally spreading the degree of redundancy over all baselines. Equation (5) can then be written as

$$\Delta T = (T_B + T_A) \left(\frac{v N_x}{B \beta \Delta \eta h} \right)^{\frac{1}{2}} w_{rms} \quad (6)$$

where we have made the approximation $\Delta \vartheta \sim \Delta \eta$; that is, the angular resolution expressed in radians is approximately equal to the angular resolution in cosine vector space. From this equation, we see that the pixel averaging afforded by the push-broom scan means that the sensitivity is independent of the number of pixels in the along-track direction (and hence of the number of antennas in the along track dimension). In practice, it may not be possible for pixel averaging to fully achieve

3. RADIOMETRIC SENSITIVITY

The radiometric sensitivity of a synthetic aperture radiometer is quoted in several forms that need to be carefully interpreted to give a consistent meaning. The general starting point in deriving the sensitivity is to derive the variance on a measurement of the fringe visibility. In synthesizing the image from the visibility functions, the variances accumulate in each pixel to give an increased variance in the apparent temperature in each pixel. The resulting standard deviations, ΔT , are scene dependent and a good approximation to a representative value of ΔT is obtained by assuming that the scene is unstructured and the measured visibilities are low.

The radiometric sensitivity may be written as¹⁴

$$\Delta T = (T_B + T_A) \left(\frac{\sum_{i=0}^N \frac{1}{r_i}}{B\tau} \right)^{\frac{1}{2}} \quad (1)$$

where T_B is the average scene temperature within the field of view of the antenna elements, T_A is the amplifier noise temperature, N is the total number of baselines and r_i is the redundancy of the i th baseline. This expression is a simplification of a more general expression and is true in the limit of an unstructured scene. In effect, each baseline adds more information to the image, but also increases the noise level. The implication is therefore that the minimum number of baselines should be employed in constructing the image. This is not necessarily true when the scene is highly structured, as is the case in astronomy. It should be noted that the area of the antennas does not appear since it is assumed that the field of view is completely filled by the Earth. The power at the output terminals of each antenna element (and consequently the variance in the measured visibilities) is therefore independent of the effective areas of the antenna elements.

It might be noted from (1) that for lowest ΔT and a non-redundant array, the number of baselines should be the smallest number that is compatible with acceptable image quality. This is the reason why sparse sampling of the support region enables lower values of ΔT to be attained than full, or denser sampling. The challenge then is to seek the value of N that gives the desired trade off of image quality against sensitivity.

Modification of equation (1) is required to account for the weighting of the visibility samples. Weighting (also known as apodisation) is necessary for low sidelobe levels. If a set of weights w_n are applied to the measured visibilities then for a single unresolved source (for which all visibilities are high), the intensity of its image must be scaled by a factor $1/w_{mean}$ where

$$w_{mean} = \frac{1}{N} \sum_{i=0}^N w_i \quad (2)$$

and the expression for the sensitivity (which can be derived by setting the signal-to-noise ratio to unity) must be multiplied by a factor w_{rms}/w_{mean} ¹⁵ where

$$w_{rms} = \sqrt{\frac{1}{N} \sum_{i=0}^N w_i^2} \quad (3).$$

However, for terrestrial observation, the images are broad and unstructured so that only very short baselines have high visibilities. For all conventional weighting schemes the weighting of these short-baseline visibilities will be very close to unity and so the sensitivity should be multiplied by a factor w_{rms} so that in place of equation (1) the sensitivity is given by

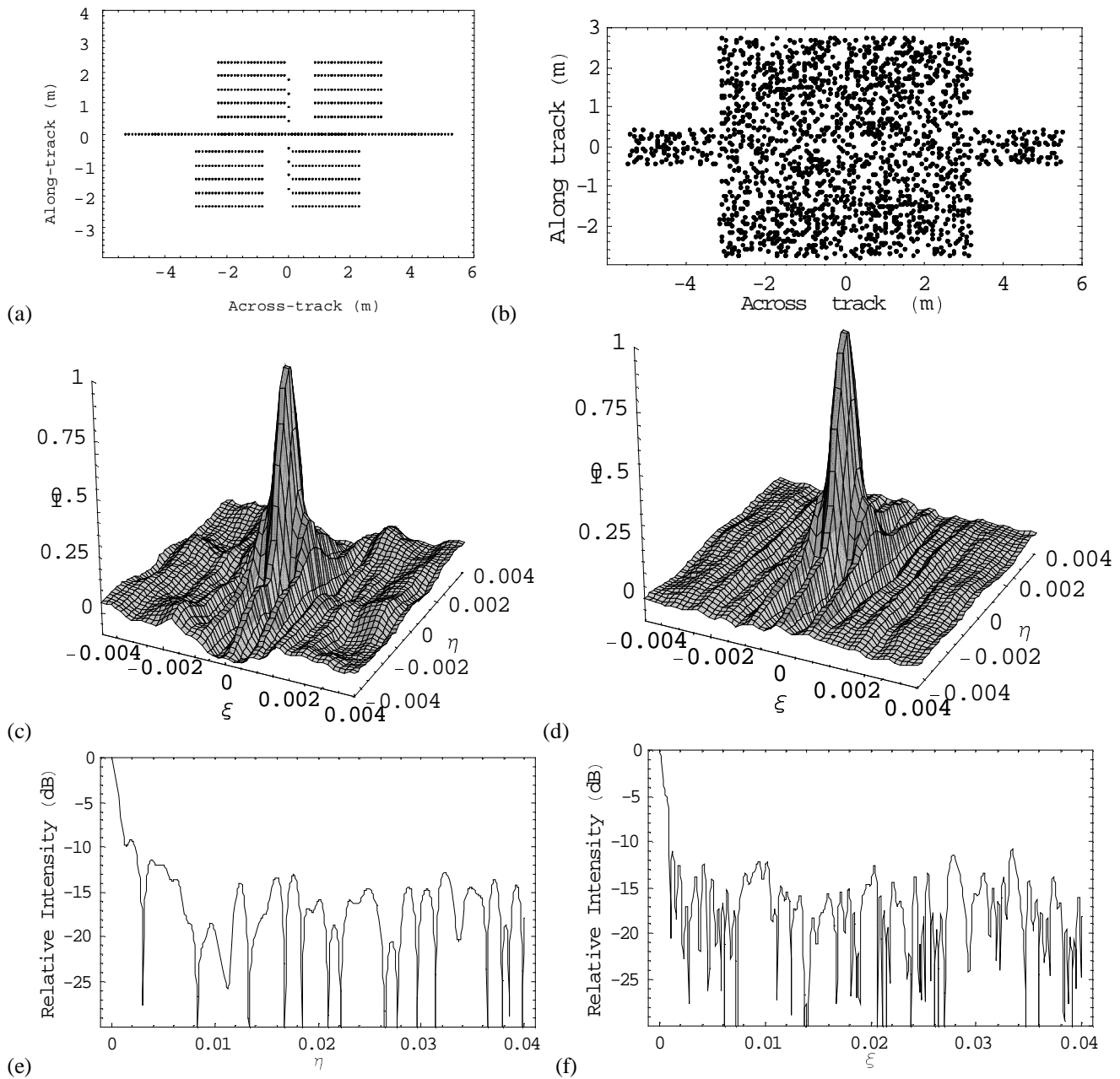


Figure 2 (a) Sampling of support region for method 1, (b) irregular sampling of support region with method 3 (c)SAIR antenna response with method 3 and 1000 samples in the support region and (d) 10,000 samples in the support region, (e) and (f) are slices along the principle axes through (c)

The design of the antenna array that gives irregular but statistically uniform coverage of the support region is not straight forward. Uniformly distributing antennas over the available mounting area on the UAV will result in a support region that is more densely sampled close to the origin. One approach to designing the antenna array may be to use optimization techniques to optimize the antenna array topology and other parameters using an appropriate cost function, such as SAIR antenna pattern

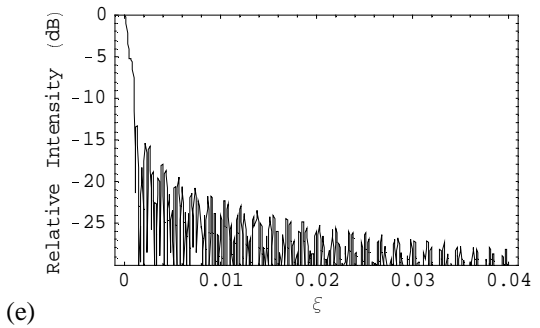
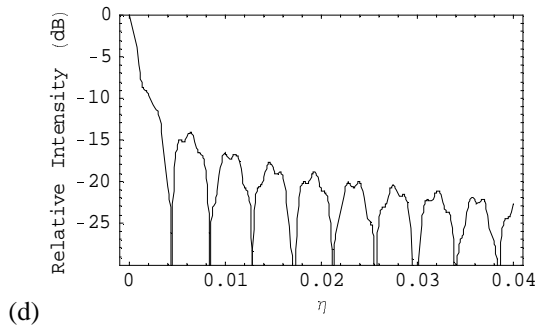
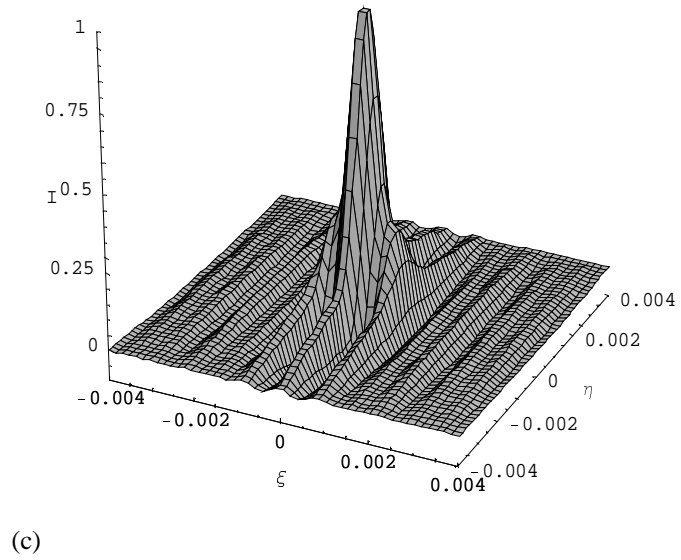
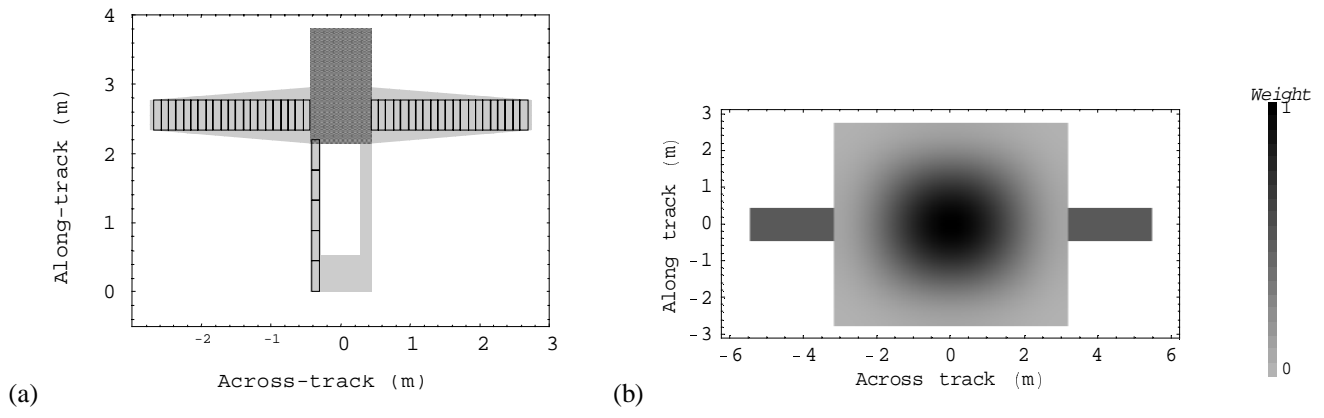


Figure 1 (a) Available real estate for mounting antennas, (b) weighted support region for this array, (c), (d) and (e) antenna patterns obtainable from this support region

2. ANTENNA PATTERN

The antenna pattern of an imager can be calculated from the Fourier transform of the autocorrelation of the antenna aperture amplitude distribution. That is, to say that the amplitudes of the scene spatial frequencies sampled by the imager are obtained from the autocorrelation function. For a filled aperture, the autocorrelation function has a smoothly varying normalized value between zero and one, whereas for a sparse synthetic aperture array with zero redundancy (that is, all antenna vector separations occur only once) the only values that occur are zero and one. This tends to result in a square law relationship between the two antenna patterns. For example, for a uniformly weighted filled antenna the autocorrelation function is a triangle function and the antenna pattern is a sinc^2 function, whereas for a sparse antenna array, the autocorrelation function is a Rect function and the antenna pattern is a sinc function. At first glance it appears that the power of two for the filled dish will result in a narrower antenna pattern with lower sidelobes than for the sparse antenna array, but in practice the Hermitian nature of the measured quantities (the complex spatial frequencies of the scene) enables the effective dimension of the aperture to be doubled and the use of an appropriate weighting function in the image reconstruction enables the sidelobes to be suppressed. These factors cancel, so that the beam width and sidelobe level of a sparse array can be equal to those of a filled array.

The autocorrelation function represents the set of vector spacings of all the antennas in the antenna array and is plotted here in a region referred to as the support region. For a filled aperture, the support region is a continuous function. When an antenna array is employed, the support region is sampled at a set of points represented by the set of vector spacings of the antennas in the synthetic aperture array. This can be illustrated by reference to Figure 1. The outline of a small UAV is shown in Figure 1 (a), where the available mounting surfaces for antennas are shaded light gray and possible locations of antennas are shown for the case of narrow field-of-view imaging. The support region for the filled antenna array is shown in Figure 1 (b) and the calculated antenna pattern is shown in Figure 1 (c) as a two dimensional plot and in (d) and (e) as sections along the ξ and η axes, where ξ and η are direction cosines parallel and perpendicular to the UAV fuselage. The weighting of the antenna support region is indicated in (b) and is given here by a Hamming weighting for the main rectangle of the support region and a constant level of 0.5 for the smaller rectangles. The optimum weighting function may be derived from a consideration of acceptable sidelobes levels and width of the main lobe, although no rigorous optimization has been applied here.

Each complex correlator in the SAIR yields measurements in the support region which enables calculation of one complex angular frequency component of the scene intensity distribution. Nyquist sampling of the scene spatial frequencies is achieved by sampling the support region at $\lambda/2$ intervals and this will yield an antenna pattern that is almost identical to that shown in Figure 1 (d) and (e). Approximately 8,000,000 correlators would be required to fully sample this support region. The inputs to these correlators could be generated by a sparse array of small antennas. For n antennas, there are $n(n-1)/2$ possible combinations so approximately 4,000 antennas and receivers will be required. This number of antennas and correlators is considered prohibitively complex and some simplification is required. This was the prime motive for proposing the three SAIR techniques mentioned in section 1.

The first of these three techniques involves Nyquist sampling of the support region in the across-track dimension and sub-Nyquist sampling in the along-track dimension. This inevitably introduces aliases (grating lobes) in this dimension that restrict the field of view to about one half of the antenna pattern width in that direction. The second technique involves sub-Nyquist sampling in both directions and results in aliases in both directions. The third technique uses random sampling of the support region. This produces no aliases and the sidelobes are noise-like and uniformly distributed across the image. As will be seen, it appears to be possible to design a SAIR with random sampling of the support region that enables an acceptable antenna pattern to be obtained from a less complex system, with a greater radiometric sensitivity. The normalized RMS sidelobe level is approximately equal to the square root of the number of independent samples in the support region. For n antennas there are $n(n-1)/2$ independent points in the support region, so for large n , the RMS sidelobe level is approximately equal to $\sqrt{2/n}$.

These points are illustrated in Figure 2. Figure 2 (a) and (b) show sampling of the support region using methods 1 and 3. It can be appreciated from comparison of Figure 1 (a) and Figure 2 (a) that there is a high degree of redundancy for the antenna array across the wings, but zero redundancy elsewhere. The reduction in sidelobe levels can be seen from comparison of Figure 2 (c), which used 1,000 samples in the support region and Figure 2 (d), which used 10,000 samples. One-dimensional sections along the principle axes of Figure 2 (c) are shown in Figure 2 (e) and (f). It might be noted that a SAIR antenna pattern has both negative and positive sidelobes, unlike the power patterns obtained from real apertures, which are always positive. In Figure 2 (e) and (f), the modulus of the antenna pattern has been taken. The full width at half maximum (FWHM) widths of the antenna patterns are $\Delta\xi=0.0007\approx 0.04^\circ$ across track and $\Delta\eta=0.0014\approx 0.08^\circ$ along track for all antenna patterns.

dimensional image. Other candidate techniques are the closely related RadSAR⁸ and supersynthesis⁹ techniques, the Mills Cross¹⁰ and hybrid techniques combining a slow conical scan with one- and two-dimensional aperture synthesis such as the so-called QUARTZ technique¹¹. In seeking to extend these microwave SAIR techniques to mm-wave frequencies it is crucial to consider the ramifications of operation at higher mm-wave frequencies in terms of the increased demands on component specifications and the greatly increased costs.

For military surveillance, aperture synthesis offers the potential for passive mm-wave imaging from antenna arrays that can be two dimensional or even conformal to the structure of a military vehicle. Aperture synthesis what is probably the only realistic route to high-resolution passive mm-wave imaging from aircraft such as a UAV. The basic concept is to mount the array of antennas onto the structure of the UAV so that an antenna is synthesized with a resolution similar to that of a filled antenna with the length and breadth of the UAV. However to make this technique work requires careful consideration if useful detection, recognition and identification (DRI) performance is to be achieved from a system that can be realistically be built at an acceptable cost. We propose here a top level design for such a system.

The most important SAIR parameters include radiometric temperature sensitivity, field of view and complexity. In general the first two parameters can only be improved with a cost and complexity penalty. For remote sensing from a satellite it is possible to achieve a very good ratio of sensitivity to complexity using one-dimensional aperture synthesis with a fan beam¹² similar to that proposed by the ESTAR program. However, this requires an antenna array that is incompatible with deployment on an aircraft and we describe here alternative approaches. Several techniques have been considered¹³ and the techniques that have received most attention here are variations on two-dimensional aperture synthesis. This technique offers the possibility of real-time calibration of a flexing antenna array and the main challenge is to achieve useful performance with acceptable complexity and cost.

To implement passive mm-wave imaging from a SAIR mounted on a UAV platform, the following challenges must be addressed:

- The antenna pattern of the SAIR must be well behaved.
- Sensitivity must be adequate
- It must be possible to calibrate the array in real time.
- It must be possible to integrate the antenna array and signal harness into the UAV structure without adversely effecting its aerodynamics and function.
- The SAIR should ideally have electromagnetic compatibility with the data link and other sensors, such as SAR.

In this article we calculate the antenna patterns that can ideally be achieved with an array of antennas mounted onto the real estate that appears to be available on a typical small UAV and a typical large UAV. In both cases it appears that antenna patterns can be formed that have acceptable sidelobe levels and a narrow main beam. The achievable angular resolutions are comparable to that of a current wide field-of-view thermal imager. An operational center frequency of 80 GHz has been assumed since this offers the good foul-weather scene contrast and the possibility of exploiting low-cost commercial off-the-shelf radio-frequency components developed for the automotive radar market.

Three approaches to deployment of a SAIR on a UAV were identified as the most promising, these are:

1. Wide field-of-view across-track imaging, with narrow along-track field of view using a filled regular array of narrow stick antennas across the wings and along the fuselage. The antennas are aligned with the fuselage and the array shape is approximately a 'T' or a cross. There are no aliases in the across-track direction, but there are aliases in the along track dimension.
2. As above, except the stick antennas are wide, so that the field of view is narrowed in the across-track dimension. In principle the antennas may be electronically scanned across the field of regard of the swath width.
3. Wide field-of-view imaging using irregular arrays of small feed-horn antennas with sparse, irregular sampling of the spatial frequencies in the scene.

In section 2 we discuss the antenna pattern that can be achieved from the available real estate on a typical UAV and how closely this might be approached by the candidate SAIR techniques. In section 3, we describe the calculation of the radiometric sensitivity and in section 4 we present system-level calculation of important system parameters for each of the three SAIR techniques outlined above. In section 5 we discuss how the SAIR may be calibrated and conclusions are presented in section 6.

Prospects for mm-wave aperture synthesis from space-borne and aerial platforms

A.R. Harvey ^{*a}, R Appleby ^b

^aDepartment of Aerospace, Power and Sensors, Cranfield University, Shrivenham,
Swindon, SN6 8LA, UK

^bDERA, St Andrews Rd., Malvern, Worcestershire, WR14 3PS

ABSTRACT

Passive imaging using mm-waves offers very significant advantages in scientific and military surveillance. However, the relatively long wavelengths mean that for the resolutions that are sought, the input aperture of the imager needs to be quite large, typically in excess of one meter. Deployment of conventional dish antennas of these dimensions on aircraft and in Low Earth Orbit is highly problematic. The use of snapshot synthetic aperture interferometric radiometry (SAIR) offers an attractive route to integrating a two-dimensional antenna array into the structure of an aircraft so that the transverse dimensions of the antenna can be almost as large as the aircraft. We report here a study into the feasibility of deployment of a SAIR on unmanned airborne vehicles and the achievable performance parameters. The critical considerations are the achievement of acceptable sensitivity and angular resolution from a SAIR that does not require excessive complexity. It is shown that traditional approaches based on fully sampling the spatial frequencies in the scene are unable to simultaneously meet all of these criteria, but that a SAIR based on thinned sampling of the spatial frequencies shows promise.

1. INTRODUCTION

Recent years have witnessed a growing interest in passive microwave and millimeter wave imaging for military and scientific applications. The military interest arises principally from the ability of mm-waves to penetrate poor weather and obscurants such as cloud, fog dust and smoke in both day and night operations. Scientific applications include aerial and space-based remote sensing of geophysical features, such as measurement and classification of snow and ice cover¹, sea and land surface temperatures, sea surface salinity, soil moisture content and wind velocity². Mechanically scanned mm-wave imagers, such as MERIT³ and MITRE (developed for military surveillance by DERA in the UK) and space-borne instruments such as AMSR and SMMR have previously been demonstrated, but for angular resolutions substantially less than 1 milliradian, deploying the large antennas required becomes increasingly problematic. We address here the design of a thinned-array synthetic aperture interferometric radiometer (SAIR) for imaging from small aerial platforms such as unmanned airborne vehicles (UAVs). The results presented are also pertinent to deployment of SAIRs on space platforms.

Mm-wave SAIR for Earth observation has great promise for terrestrial real-time mm-wave imaging^{4,5} for applications such as detection of land mines, foul weather flying aids and surveillance. The fundamental principles of aperture synthesis radiometry were developed earlier this century by optical and radio astronomers, who used several days of observing time to form a single image. Recently the techniques have been further developed by the Earth observation community with an emphasis on 'snap-shot' imaging in which a single image is formed from a single observation. Aperture synthesis is currently the only feasible technique for high-resolution passive mm-wave imaging from UAVs. These techniques are also of interest in Earth observation since they offer potential for deploying the required large apertures in Earth orbit without the large mass associated with conventional dishes. In addition, the optical aberrations that limit the field of view of dish antennas are absent, so swath widths are theoretically limited only by the reduced resolution caused by foreshortening of the antenna aperture.

The most mature research programs for Earth observation using radio-frequency aperture synthesis are ESA's MIRAS program⁶ and NASA's ESTAR program⁷ that both operate at L-band. The former uses a two-dimensional Y-shaped array of circular antennas whereas the latter employs a linear array of stick antennas that is push-broom scanned to form a two-

* Correspondence: Email: a.r.harvey@rmcs.cranfield.ac.uk,
WWW: http://www.rmcs.cranfield.ac.uk/departments/daps/Groups/Electro_optics/harvey.htm;
Telephone: +44 (0)1793 785215; Fax +44 (0)1793 785902